Electronic Supporting Information

Probing the Active Sites of Oxide Encapsulated Electrocatalysts with Controllable Oxygen Evolution Selectivity

William D. H. Stinson[a], Robert S. Stinson[a], Jingjing Jin[a], Zejie Chen[b], Mingjie Xu [c], Fikret Aydin[d], Yinxian Wang[a], Marcos F. Calegari Andrade[d], Xiaoqing Pan[c][e][f], Tuan Anh Pham[d], Katherine E. Hurst[g], Tadashi Ogitsu[d], Shane Ardo[b][e][h], and Daniel V. Esposito[a]

[a] Department of Chemical Engineering, Columbia Electrochemical Engineering Center, Lenfest Center for Sustainable Energy

Columbia University in the City of New York; New York, NY 10027 United States

[b] Department of Chemistry,

University of California, Irvine; Irvine, California 92697, United States

[c] Irvine Materials Research Institute (IMRI),

University of California, Irvine, 92697, United States

[d] Materials Science Division,

Lawrence Livermore National Laboratory; Livermore, California 94550, United States

[e]Department of Materials Science and Engineering,

University of California, Irvine; Irvine, California 92697, United States

[f] Department of Physics and Astronomy,

University of California, Irvine; Irvine, California 92697, United States

[g] Energy Conversion and Storage Systems Center

Renewable Energy Laboratory; Golden, CO 80401, United States

[h]Department of Chemistry and Biomolecular Engineering,

University of California, Irvine; Irvine, California 92697, United States

***Corresponding Author**: de2300@columbia.edu

Supporting Information Table of Contents

Section **Page**

SI. AFM

Atomic force microscopy (AFM) was performed on as-made electrodes over a 500 nm by 500 nm area. Representative images for bare Ir, SiO_x|Ir and TiO_x|Ir electrodes are shown in **Figure S1**. All three samples exhibit 50-300 nm grains, which are associated with the underlying FTO substrate. These crystallites are also directly seen in cross-sectional TEM images (**Figure S2**). Quantitative analysis of the AFM measurements was performed using NanoScope Analysis software. The root mean square (RMS) roughness was averaged for three different locations and determined to be 38 nm for bare Ir, 31 nm for the high concentration SiO_x|Ir electrode, and 35 nm for the high concentration TiO_x|Ir electrode. Additionally, the difference between the maximum and minimum height, referred to henceforth as the maximum height difference (MHD), was 278 nm for the bare Ir electrode, 243 nm for the TiO_x|Ir electrode, and 200 nm for the SiO_x|Ir electrode. The reduced RMS roughness and MHD of the encapsulated electrodes compared to the unencapsulated electrodes provides evidence of non-uniform thickness of the overlayer with increased thickness in the cavities of the Ir-coated substrate and reduced thickness on the peaks of the FTO grains.

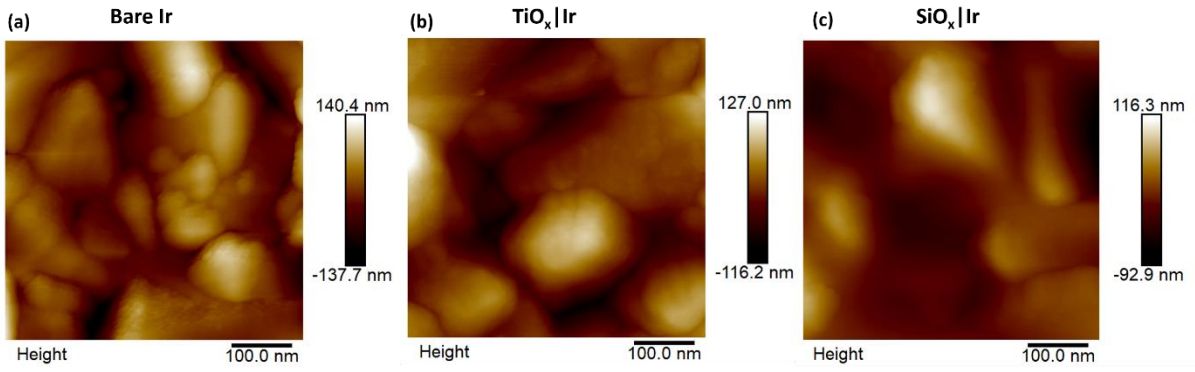

Figure S1. (a), **(b)**, and **(c)** Representative AFM images of a bare Ir, high concentration TiO_x|Ir and high concentration SiO_x|Ir electrode.

SII. Additional TEM/EDS images

To better characterize the overlayer thickness, elemental line scans were produced from the TEM/EDS elemental maps in **Figure 1, Figure 2, Figure S3-6** for the electrodes fabricated using the high precursor concentrations and **Figure S8-11** for the low precursor concentrations. In **Figure S3a,e**, the teal and white lines correspond to the locations for the linescan measurements shown in **Figure S3b-d, 3f-h**. Additional line scans were taken at three different locations and magnifications as shown in **Figures S4-6**. In all cases, the linescans reveal the transition from high Ti or Si signal associated with the oxide overlayer to Ir signal associated with the Ir thin film and finally Sn associated with the FTO substrate. The distance over which these transitions between layers occur varies significantly from location to location, which can be attributed to the 3-dimensional morphology of the interfaces which are a result of the roughness of the FTO substrate. Overlayer thicknesses were estimated from these line scans to be approximately 10-15 nm for both the TiO_x|Ir and SiO_x|Ir electrodes, with larger overlayer thicknesses measured for linescans taken in regions corresponding to the cavities between the FTO grains.

High resolution bright-field images of the high concentration SiO_x and TiO_x overlayers were also analyzed to assess the crystalline character of the overlayers. A Fast Fourier Transform (FFT) was taken over the entire bright-field image to identify any nanocrystalline features, and then translated to d-spacing (**Figure S7a-e**). Direct comparison in d-spacing of the 10 largest amplitude patterns with known diffraction patterns for SiO_2, TiO_2, Ir, and IrO_2 suggest that crystalline regions correspond to Ir or IrO_2[1-4]. This conclusion was further supported by inverse FFT images (**Figure S7c,f**), of a sub-section of the diffraction pattern, which show that the nanocrystalline regions are highly correlated with the locations of Ir or IrO_2 (dark regions) in the

high resolution STEM images (**Figure S7a,c**). Collectively, these data suggest that both SiO_x and TiO_x overlayers are amorphous.

Overlayer thickness for low concentration MO_x|Ir electrodes could not directly be measured via EDS/STEM. As shown in the EDS line scans of the MO_x|Ir electrodes (**Figure S8-11**), there is no discrete M (Ti or Si) EDS signal originating from the MO_x concentrated at the outer edge of the Ir layer. Instead, the weak MO_x signal of these samples overlaps highly with the Ir signal, which we attribute to the fact that the thickness of the MO_x overlayers is significantly less than the surface roughness of the Ir|FTO substrate throughout the thickness of the cross-sectioned specimen.

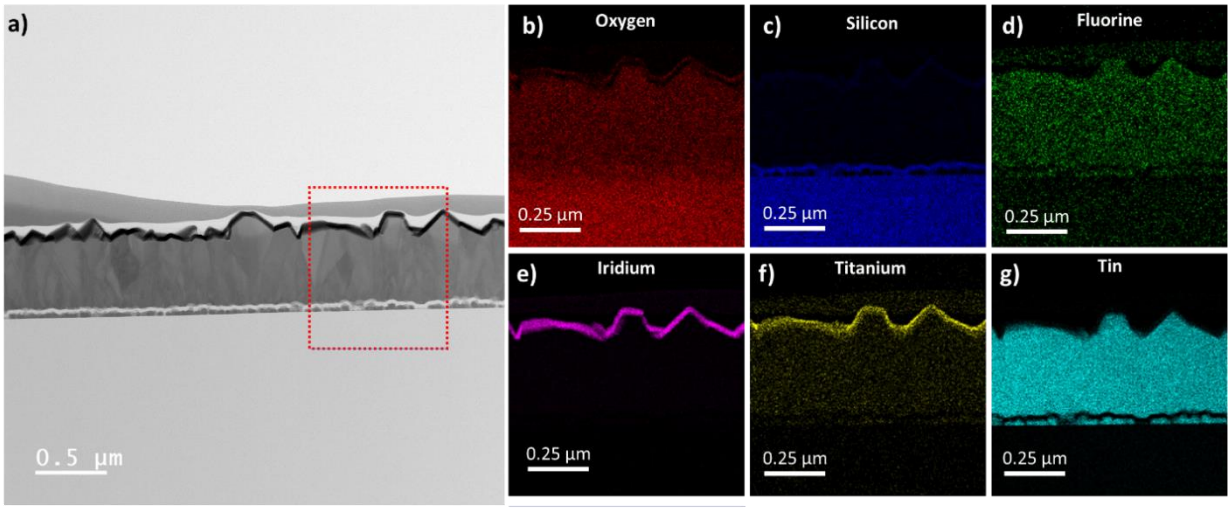

Figure S2. (a) STEM images of high concentration TiO_x|Ir|FTO with elemental composition of **(b)** oxygen, **(c)** silicon, **(d)** fluorine, **(e)** iridium, **(f)** titanium, and **(g)** tin.

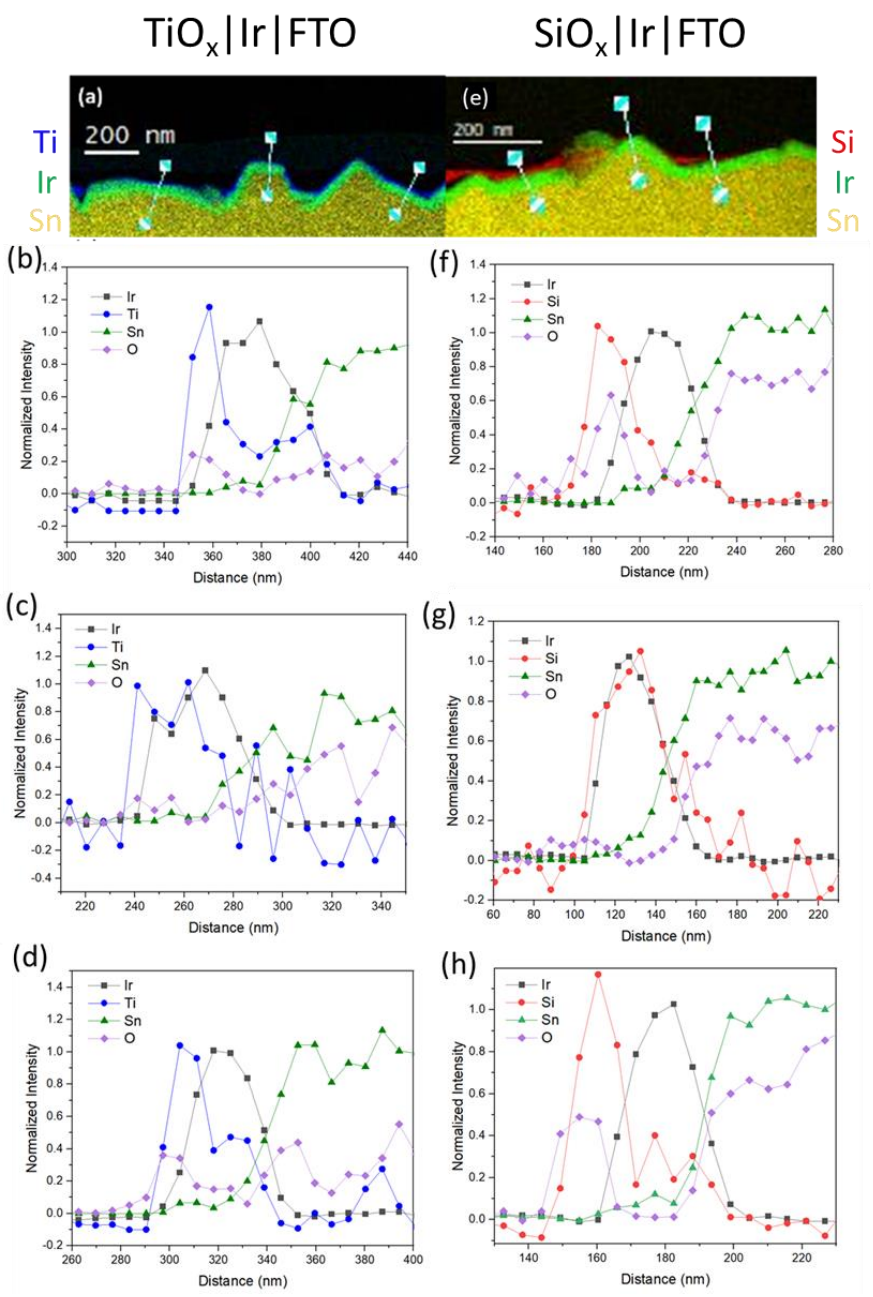

Figure S3. (a) and **(e)** STEM/EDS elemental maps of high precursor concentration TiO_x|Ir and SiO_x|Ir electrodes, respectively, with locations of three linescans indicated by teal and white lines, from left to right, as **(b)**, **(c)**, and **(d)** for TiO_x|Ir and **(f)**, **(g)**, and **(h)** for SiO_x|Ir.

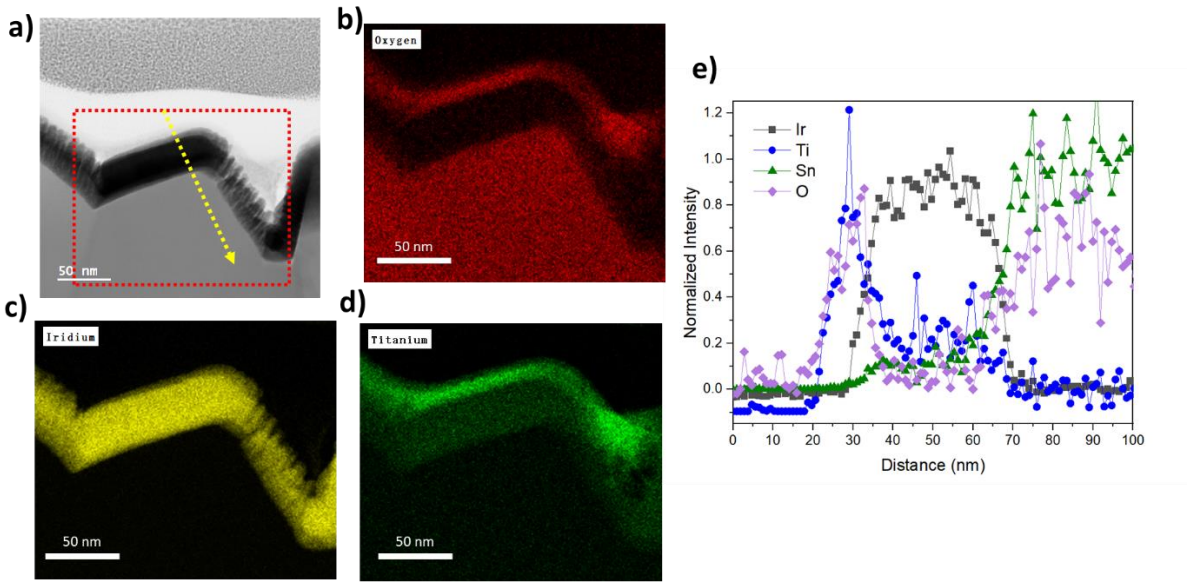

Figure S4. (a) STEM images of high concentration TiO_x|Ir|FTO with elemental composition of **(b)** oxygen, **(c)** iridium, and **(d)** titanium shown for region corresponding to the red box in **(a)**. **(e)** Normalized elemental intensity of O, Ir and Ti along dotted yellow line in **(a)**.

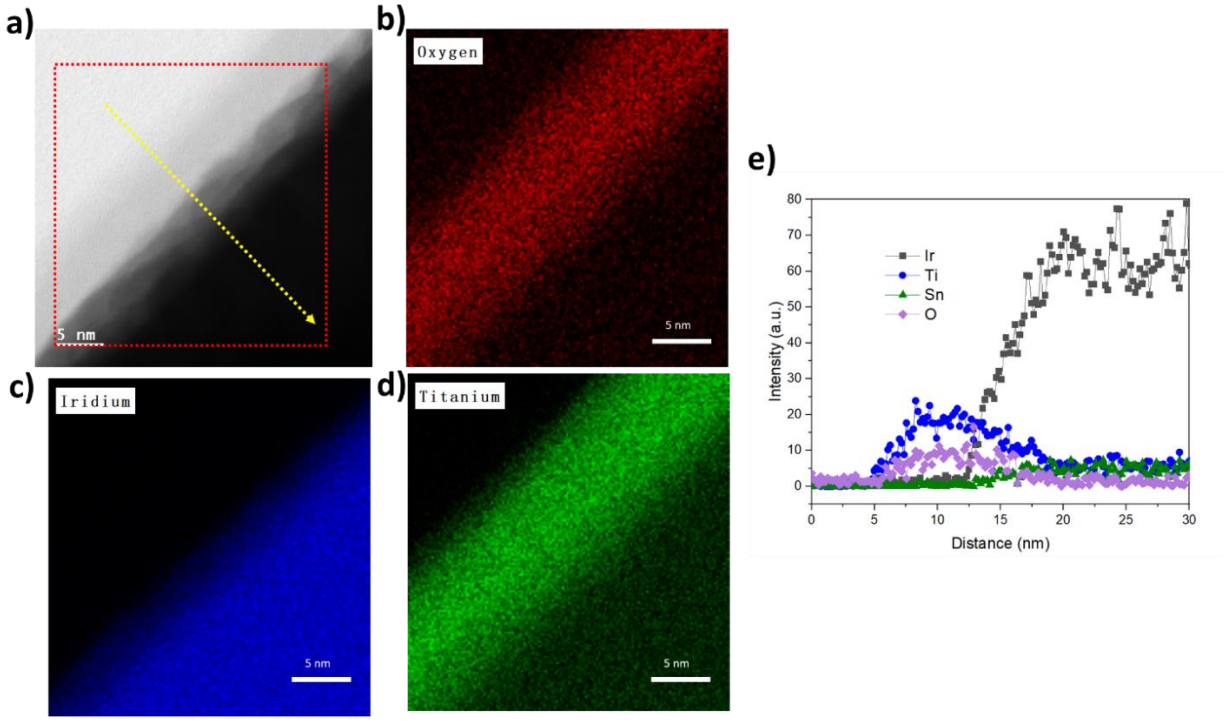

Figure S5. (a) STEM images of high concentration TiO_x|Ir|FTO with elemental composition of **(b)** oxygen, **(c)** iridium, and **(d)** titanium shown for region corresponding to red box in **(a)**. **(e)** Elemental intensity of O, Ir and Ti along dotted yellow line in **(a)**.

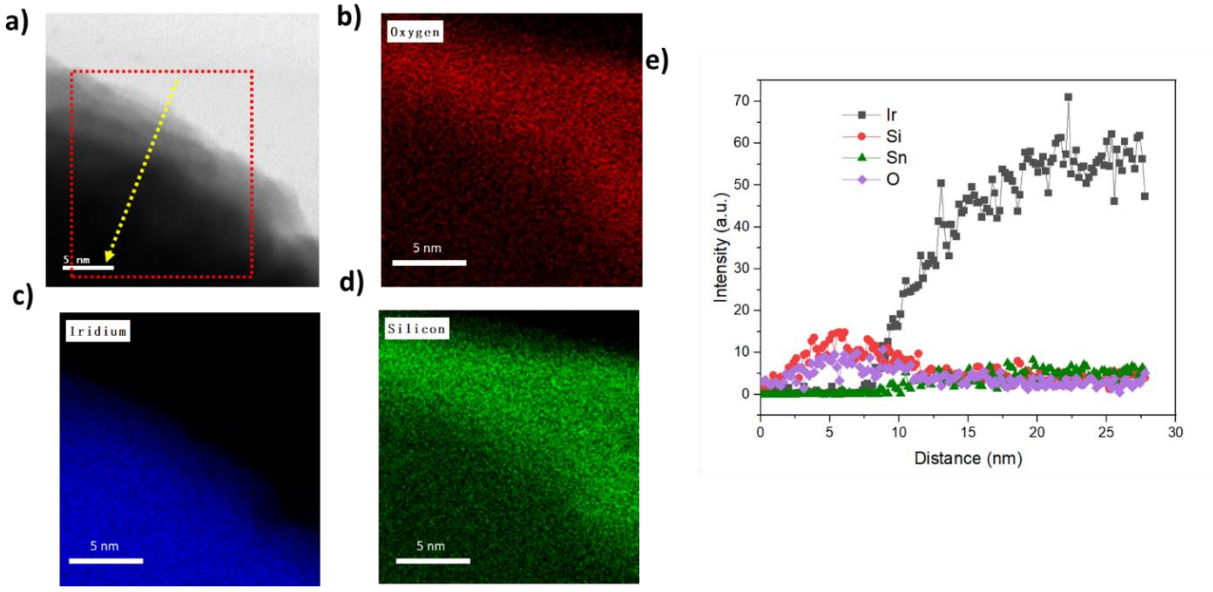

Figure S6. (a) STEM images of high concentration SiO_x|Ir|FTO with elemental composition of **(b)** oxygen, **(c)** iridium, and **(d)** silicon shown for region corresponding to red box in **(a)**. **(e)** Elemental intensity of O, Ir and Ti along dotted yellow line in **(a)**.

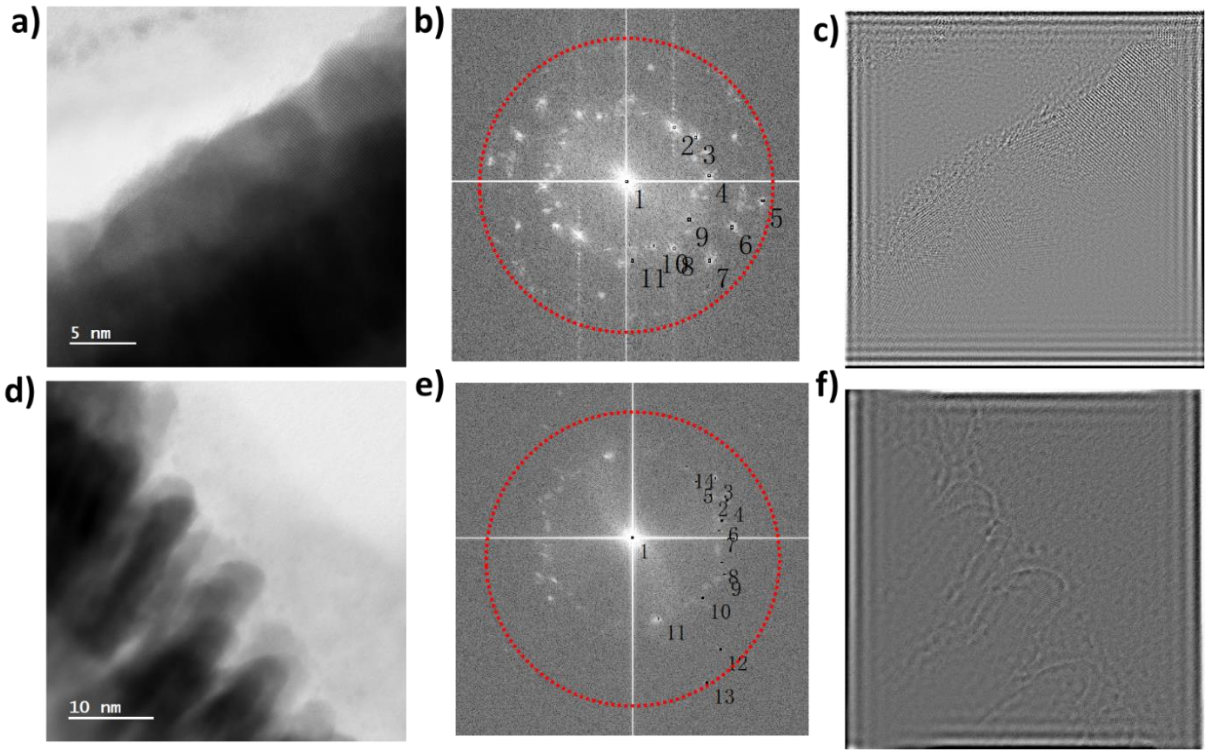

Figure S7. High resolution STEM bright-field image and Fast Fourier Transform (FFT) of high concentration **(a,b)** SiO_x|Ir and **(d,e)** TiO_x|Ir, respectively. **(c,f)** Respective inverse FFT of the nanocrystalline region only, obtained by masking amorphous regions outside of red circle in **(a,d)** using the bandpass method, showing that nanocrystalline regions correlate with locations of Ir/IrO_x.

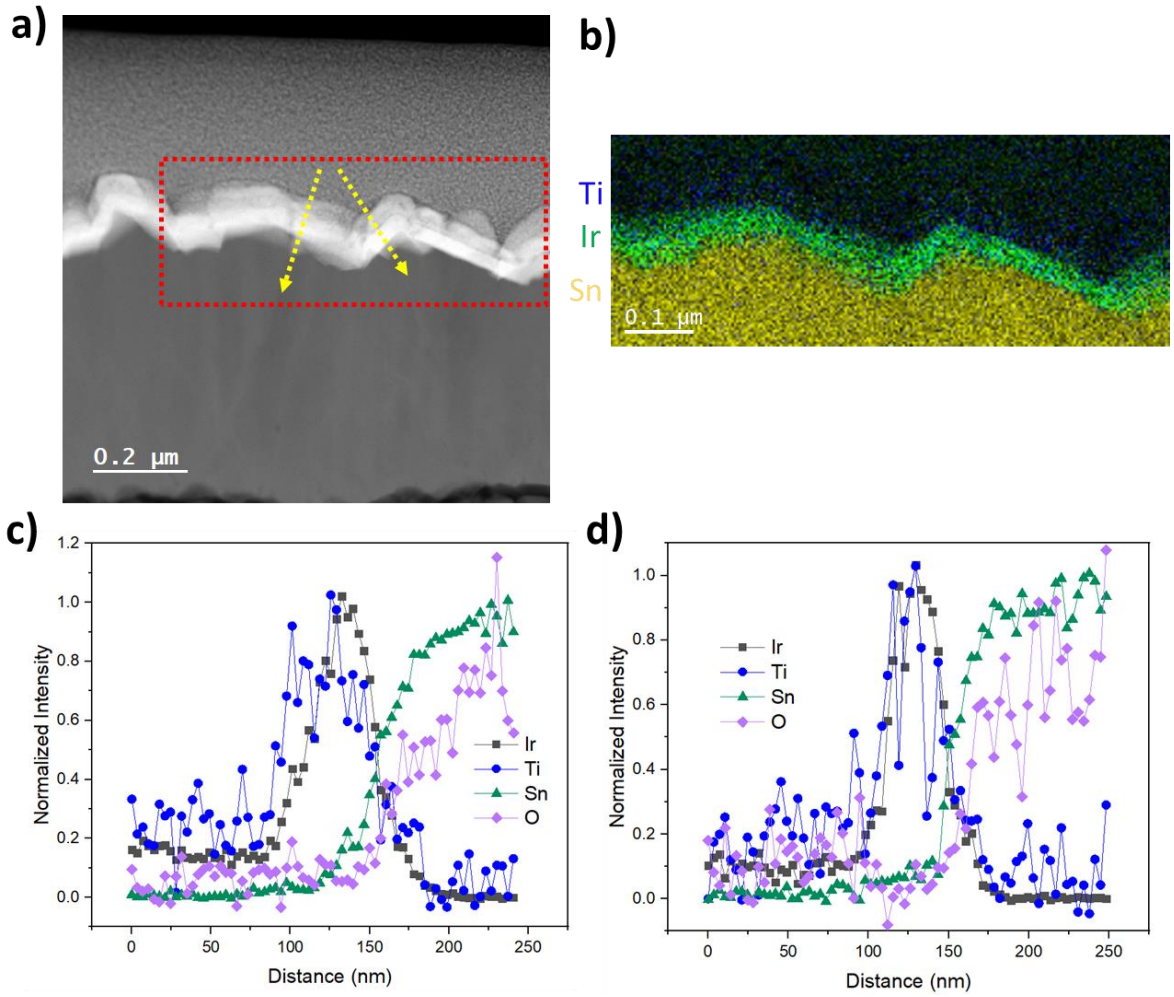

Figure S8: **(a)** STEM of the low precursor concentration TiO_x|Ir|FTO electrode with **(b)** region of EDS elemental analysis highlighted as red box in **(a)**, with elements of Sn, Ir and Ti corresponding to yellow, green, and blue, respectively. **(c,d)** Representative linescans, indicated by yellow lines in (a), from left to right, as **(c)** and **(d)**.

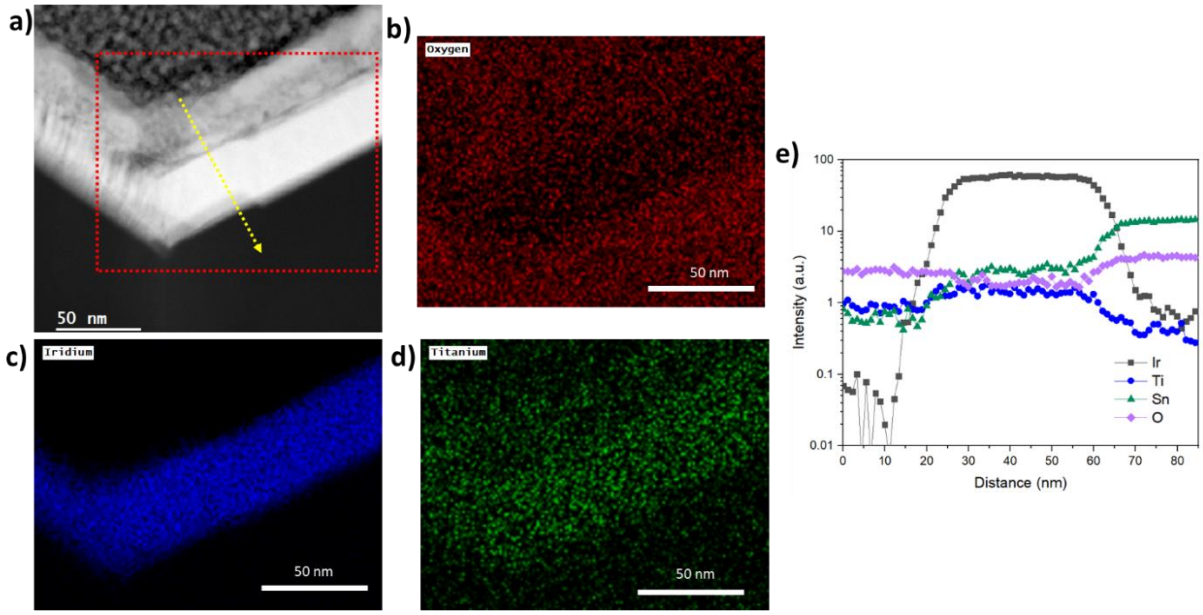

Figure S9: **(a)** STEM images of the low concentration TiO_x|Ir|FTO electrode with elemental composition of **(b)** oxygen, **(c)** iridium, and **(d)** titanium shown for region corresponding to red box in **(a)**. **(e)** Elemental intensity of O, Ir and Ti along dotted yellow line in **(a)**.

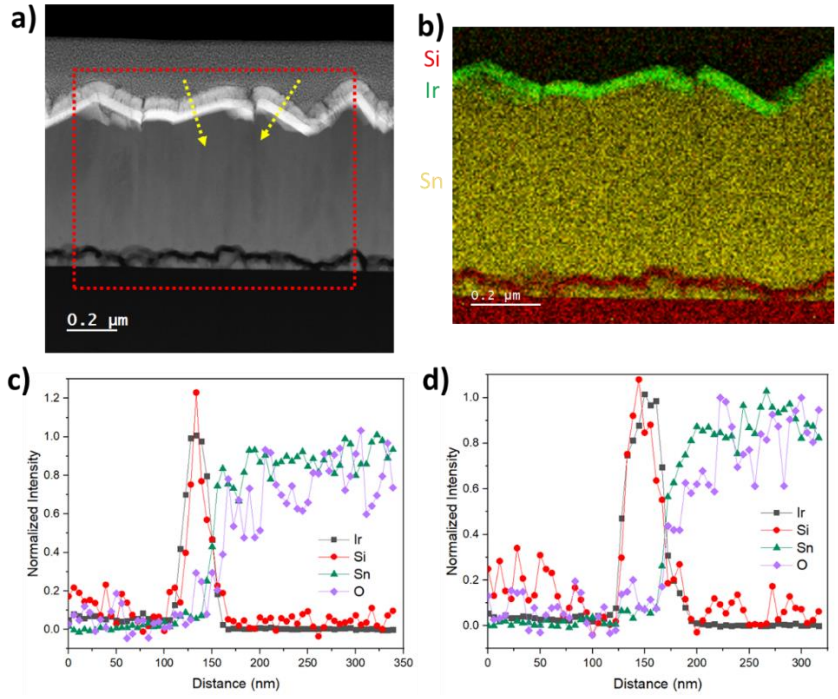

Figure S10: **(a)** STEM of the low precursor concentration SiO_x|Ir|FTO electrode with **(b)** region of EDS elemental analysis highlighted as red box in **(a)**, with elements of Sn, Ir and Si corresponding to yellow, green, and red, respectively. **(c,d)** Representative linescans, indicated by yellow lines in (a), from left to right, as **(c)** and **(d)**.

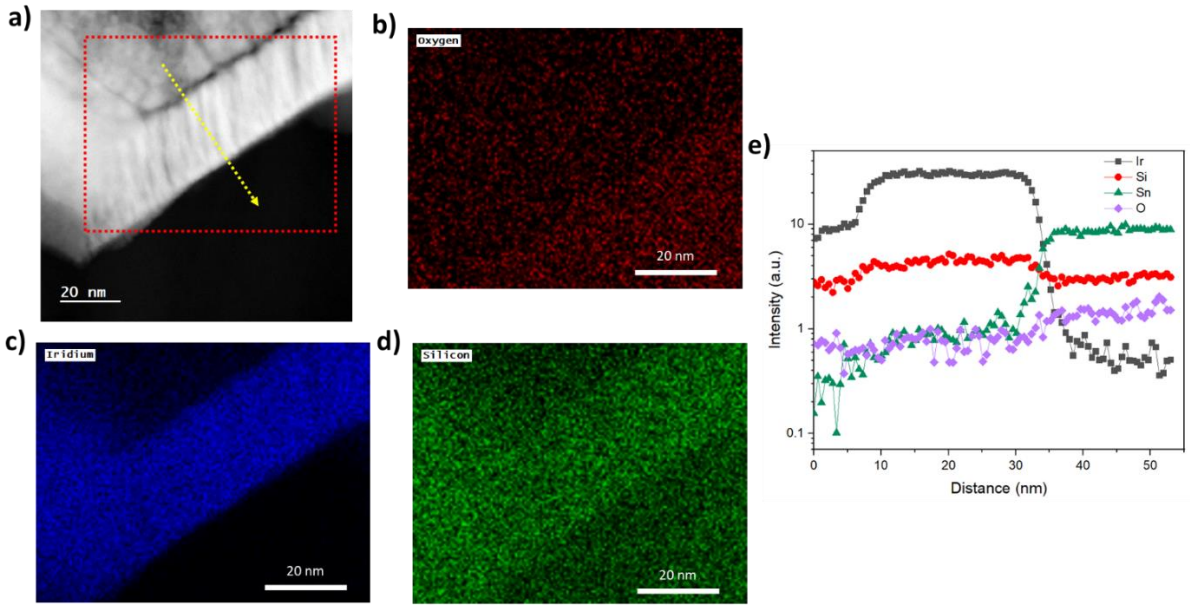

Figure S11: (a) STEM images of the low concentration SiO_x|Ir|FTO electrode with elemental composition of **(b)** oxygen, **(c)** iridium, and **(d)** silicon shown for region corresponding to red box in **(a)**. **(e)** Elemental intensity of O, Ir and Si along dotted yellow line in **(a)**.

SIII. XPS

X-ray photoelectron spectroscopy (XPS) measurements were completed using a Phi 5500 XPS system with a monochromatic Al Kα source (15 kV, 20 mA) and a base pressure of < 2 x 10^{-10} Torr with a charge neutralizer, tilted to 54.7º relative to the detector. No additional shifts to the binding energy scale were applied during post processing. All multiplex scans were measured for three cycles over the regions of interest with a step size of 0.05 eV, dwell time of 655 ms, and pass energy of 23.5 eV.

Scans were analyzed using CasaXPS software. A Shirley model was used to fit the background of all spectra. Ir 4f peaks, both metallic and IrO_x, were fitted using a Functional Lorentzian peak shape, and constrained for 7/2 -5/2 peak splitting of 2.98 eV and 0.75 area outlined in [5]. O 1s peaks associated with the IrO_x species were additionally fitted with the same line shape as Ir 4f peaks. O 1s peaks associated with Ti-O and Si-O were fitted with a Gaussian–Lorentzian line shape, with 70% Gaussian behavior. Si 2p and Ti 2p peaks were also fit with a Gaussian–Lorentzian line shape, with 70% Gaussian behavior and full width at half maximum (FWHM) constrained to be < 2. It was found that the Ti 2p region could not be fitted with a single doublet, so it was fitted with two doublet peaks each with a 1/2-3/2 peak splitting of 5.72 eV and area ratio of 0.5. The two doublet peaks, commonly associated with Ti^{4+} (from TiO_2) and Ti^{3+} (either from Ti-OH or Ti neighboring oxygen vacancies), had a similar difference in binding energies as seen previously in literature [6, 7]. The O 1s region for the TiO_x|Ir electrode required two peaks to fit the region, which is consistent with oxygen incorporated in the TiO_x lattice (Ti-O-Ti) and surface oxygen (seen as either Ti-OH or adsorbed H_2O). The C 1s region for high concentration MO_x|Ir and bare Ir samples can be seen in **Figure S13**. C1s spectrum were not shifted, as carbon signal

could originate from both the outer surface as well as the buried interface. C 1s peaks were fit with a Gaussian–Lorentzian line shape, with 70% Gaussian behavior and FWHM constrained to be < 2. A singular peak was fit for the bare Ir, while additional peaks were needed to fit the region for high SiO_x|Ir and TiO_x|Ir electrodes, respectively. These higher binding energy peaks are typically associated with single and double C-O bonds[8], but could originate from partially reacted precursors at the thickest MO_x locations[9]. XPS for an additional bare Ir sample, which underwent 120 minutes of UV-ozone treatment (identical to that used for MO_x|Ir electrodes), is also shown in **Figure S12**.

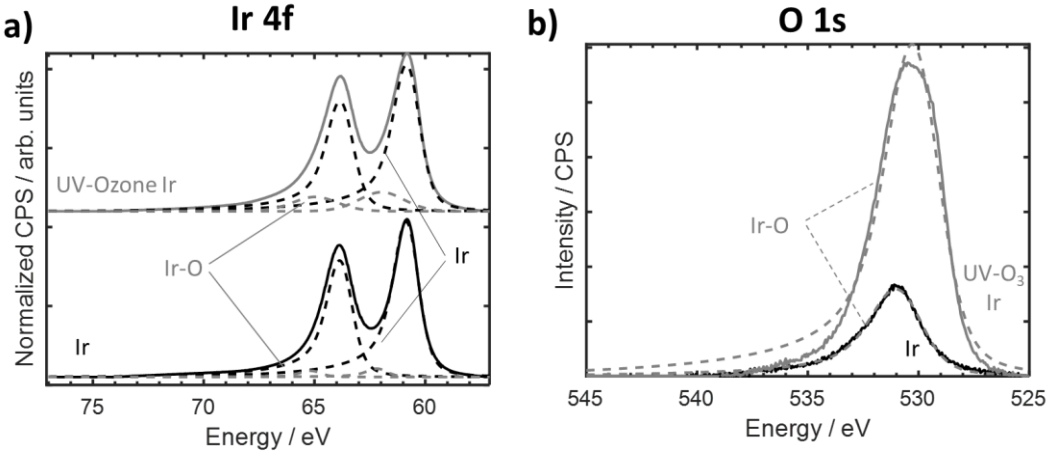

Figure S12. XPS of Ir sample that underwent oxidation through the UV-ozone process used to convert MO_x samples. **(a)** Ir 2f (normalized CPS) and **(b)** O 1s regions (raw intensity).

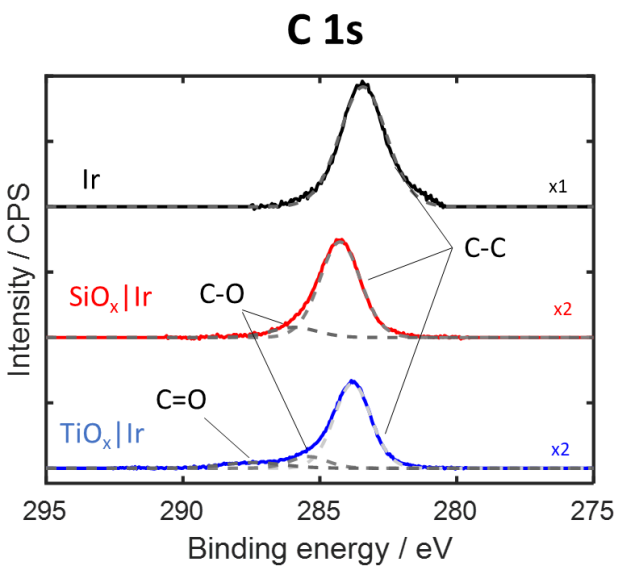

Figure S13. C1s spectra of bare Ir, high concentration TiO_x|Ir and high concentration SiO_x|Ir substrates seen in Figure 3 in the main article.

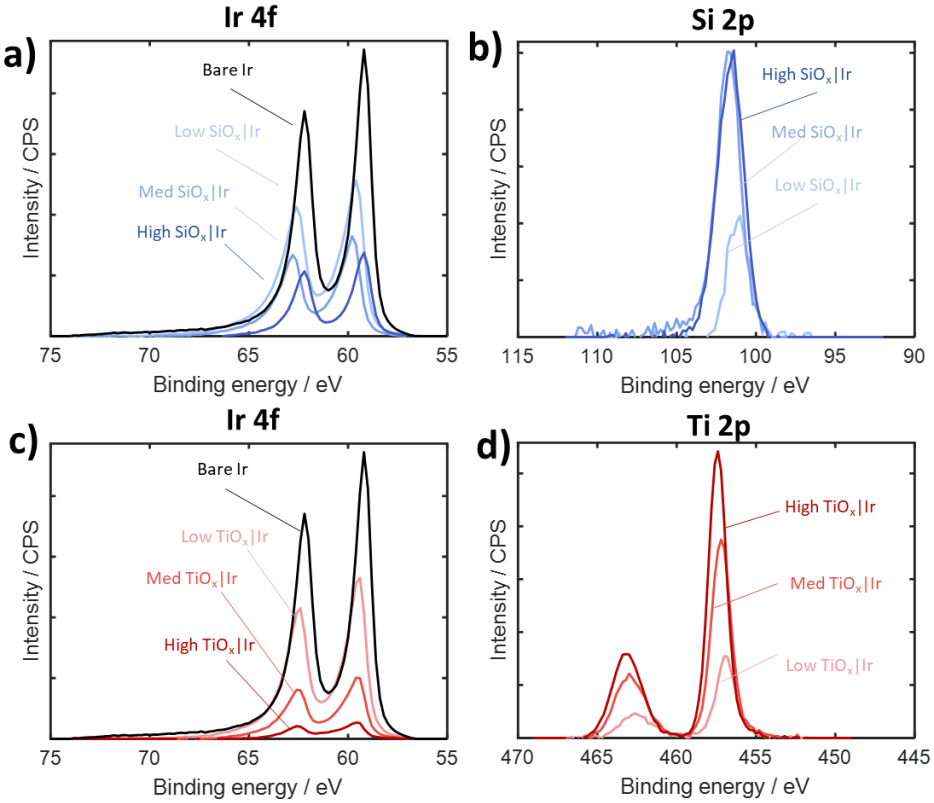

Figure S14: XPS scans of **(a,b)** SiO_x|Ir and **(c,d)** TiO_x|Ir samples of varying precursor concentrations ("Low", "Med.", "High"), with **(a,c)** Ir 4f, **(b)** Si 2p and **(d)** Ti 2p regions.

SIV. Additional Cyclic Voltammograms of MO_x|Ir

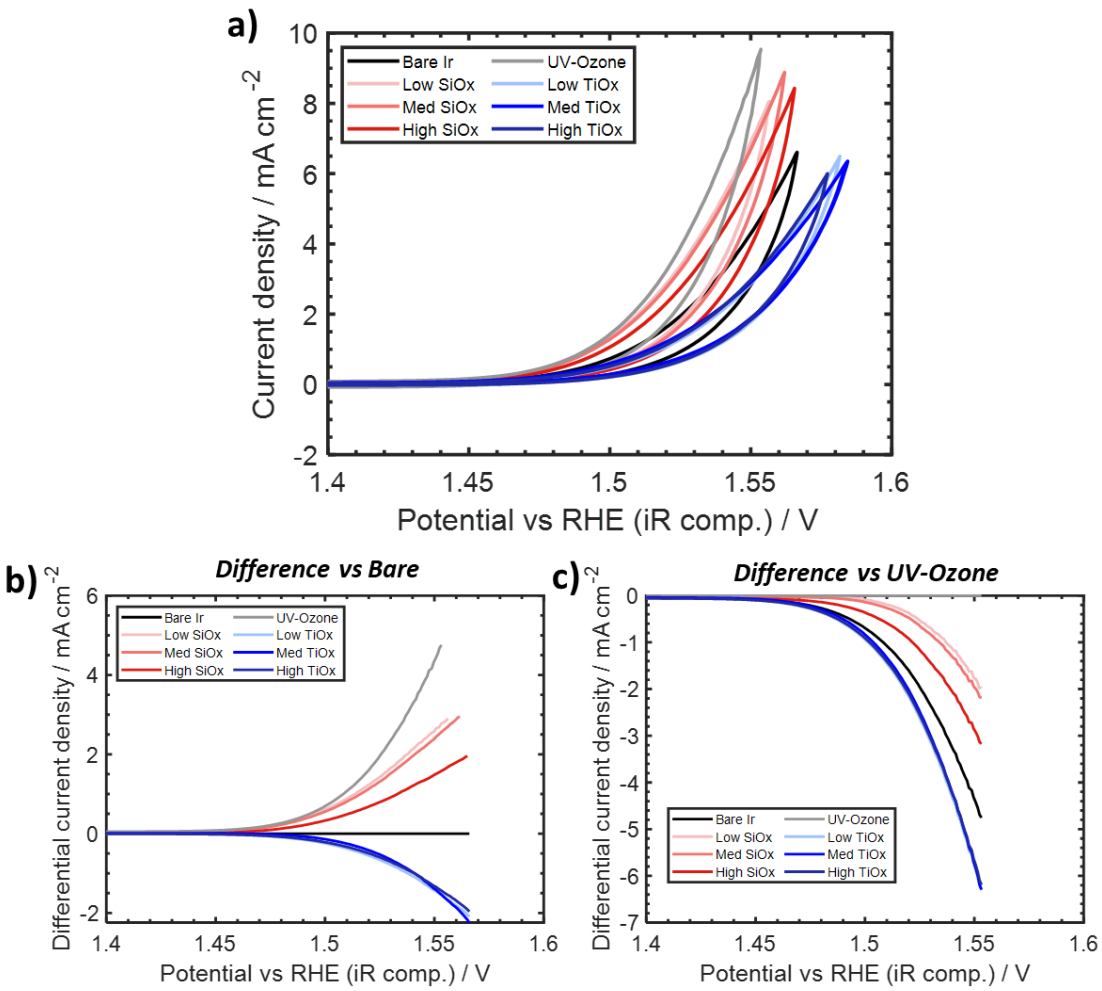

Figure S15. (a) CV measurements for varying overlayer concentrations (low, medium, high) of SiO_x|Ir and TiO_x|Ir electrodes in deaerated aqueous 0.1 M Na_2SO_4 + 0.05 M H_2SO_4 supporting electrolyte at 20 mV s-1 (iR corrected). Differential CV curves were generated by subtracting the current density for MO_x|Ir electrodes from the current density at each potential for the **(b)** bare Ir electrode and **(c)** UV-Ozone treated bare Ir electrode at each potential.

Table S1: OER overpotential of MOx|Ir samples from CV measurements in supporting electrolyte (50 mM H2SO4 + 100mM Na2SO4) and Fe containing electrolyte (25 mM $FeSO_4$ + 12.5 mM $Fe_2(SO_4)_3$ + supporting electrolyte), pH 1.5, iR corrected)

Electrode	η_{OER} (Supporting) @ 1 mA cm^{-2} / mV	η_{OER} (Supporting) @ 4 mA cm^{-2} / mV	η_{OER} (Fe containing) @ 1 mA cm^{-2} / mV	η_{OER} (Fe containing) @ 4 mA cm^{-2} / mV
Bare Ir	283	349	333	417
UV-Ozone Ir	266	323		
Low SiO_x|Ir	266	329	310	377
Medium SiO_x|Ir	266	326	320	411
High SiO_x|Ir	273	333	283	353
Low TiO_x|Ir	293	359	313	390
Medium TiO_x|Ir	286	356	319	396
High TiO_x|Ir	293	363	326	410

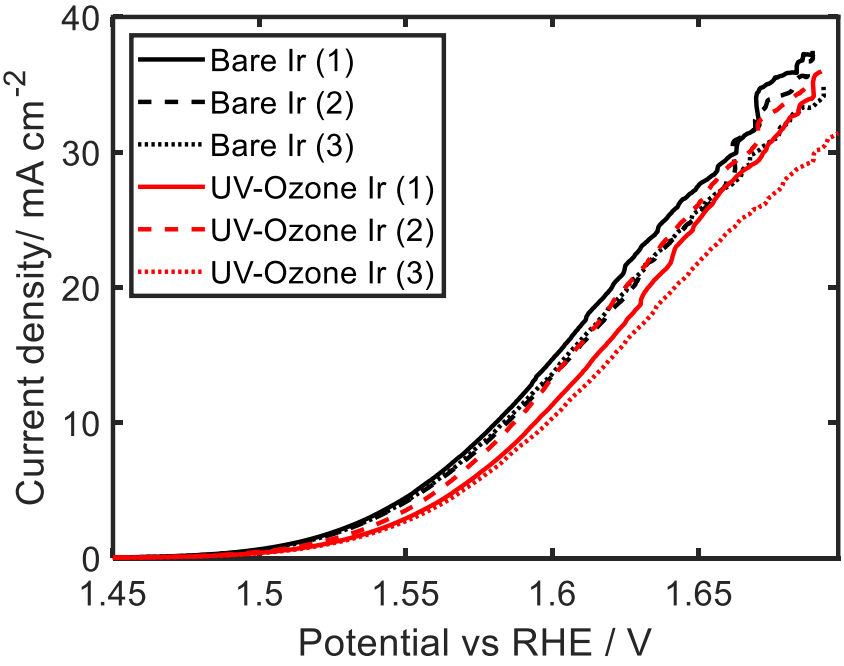

Figure S16: Linear sweep voltammograms of 3x repeats bare Ir (black traces) and UV-Ozone Ir (red traces) in 0.05 M H_2SO_4 + 0.1 M Na_2SO_4 (pH 1.5) at 5 mV s^{-1}.

SV. Tafel analysis of Ir|FTO electrodes

Tafel slopes for bare Ir, TiO_x|Ir, SiO_x|Ir electrodes were calculated between potentials of 1.455 V and 1.505 V vs RHE from supporting electrolyte scans seen in **Figure S15**, with representative curves shown in **Figure S17** for the highest precursor concentration overlayers reported in the main article**,** where the calculation region is highlighted in black. Tafel analysis was carried out on i-R corrected Tafel plots, with the series resistance determined from the high-frequency x-intercept of Nyquist plots measured by electrochemical impedance spectroscopy (EIS) for each sample. The calculated Tafel slopes are provided in **Table S2**. The Tafel slopes for all electrodes are with +/- 5 mV of each other and similar to the Tafel slopes for IrO_x electrodes previously reported in literature for acidic electrolytes[10-13].

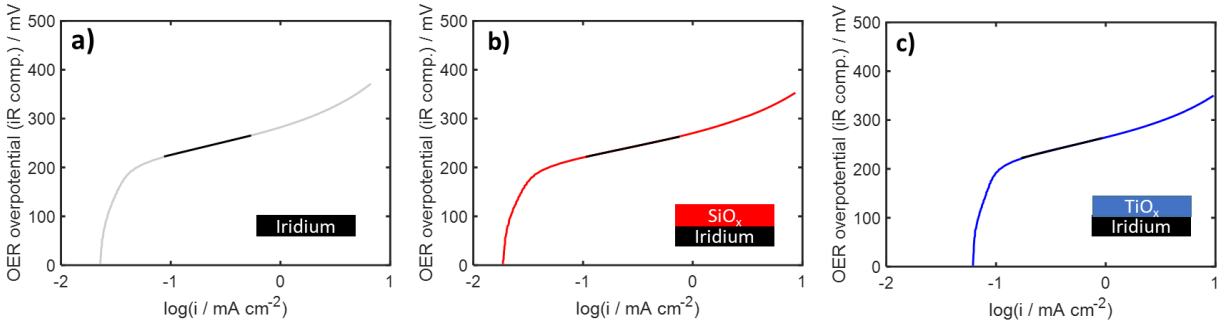

Figure S17. (a), **(b)**, and **(c)** OER overpotential vs log of current density for Ir, TiO_x|Ir and SiO_x|Ir electrodes in deaerated aqueous 0.1 M Na_2SO_4 + 0.05 M H_2SO_4 supporting electrolyte. All curves were i-R compensated for series resistance using the high frequency x-intercept of Nyquist plots measured by EIS. Black solid line represents the region of Tafel fit.

Table S2. Calculated Tafel slopes between potentials of 1.455 V and 1.505 V vs RHE for i-R compensated CVs in deaerated 0.1 M Na_2SO_4 + 0.05 M H_2SO_4 supporting electrolyte (pH 1.5), seen in Figure S12.

Electrode	Tafel Slope / mV dec^{-1}
Bare Ir	**54**
UV-Ozone Ir	**53**
2 nm SiO_x|Ir	**50**
5 nm SiO_x|Ir	**48**
10 nm SiO_x|Ir	**57**
2 nm TiO_x|Ir	**61**
5 nm TiO_x|Ir	**61**
10 nm TiO_x|Ir	**55**

SVI. Chronoamperometry of high concentration MO_x|Ir

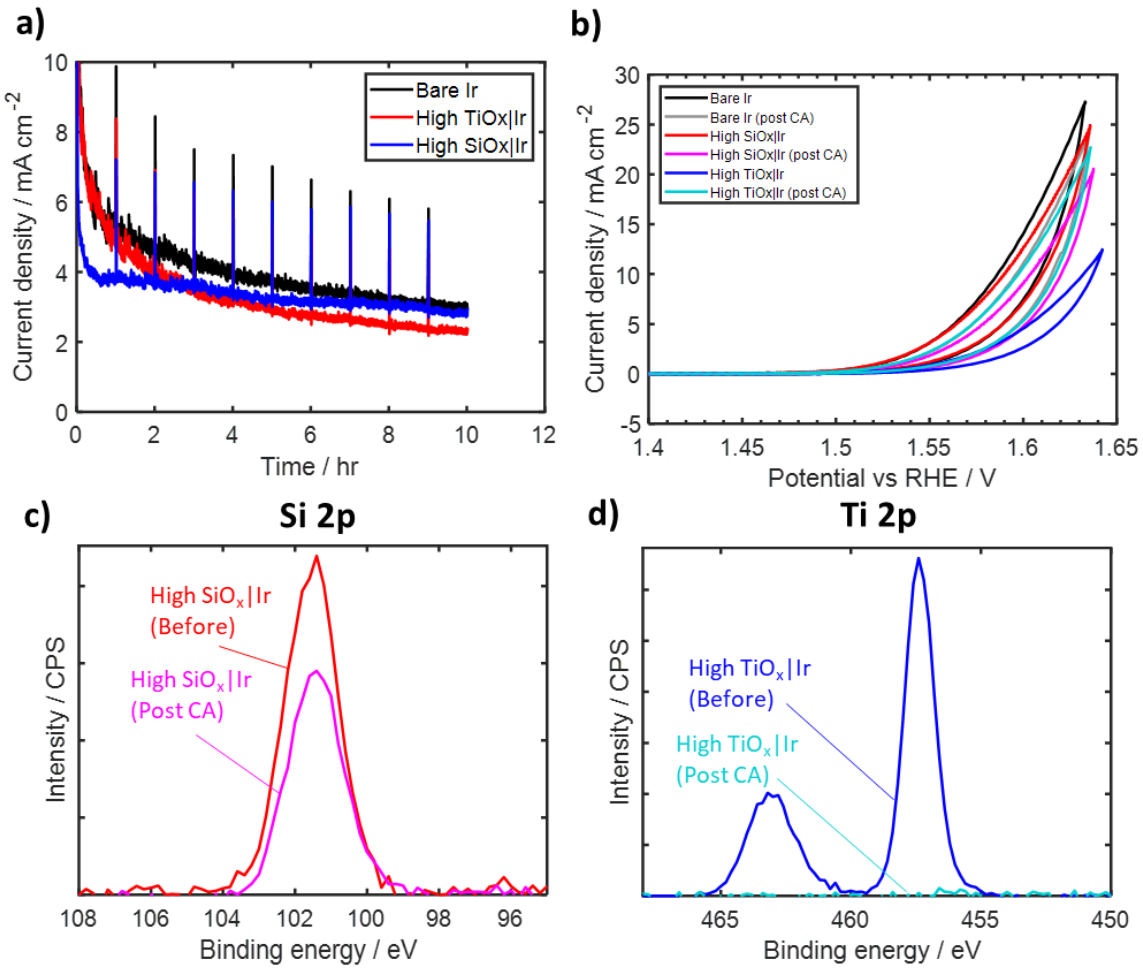

Figure S18: **(a)** Chronoamperometry scans of high concentration MO_x|Ir and bare Ir electrodes completed in 50 mM H_2SO_4 + 500 mM Na_2SO_4 (pH 1.5) at 1.65 V vs RHE (85% iR compensated). **(b)** Representative cyclic voltammograms taken at 20 mV s^{-1} of electrodes before and after CA experiment in same electrolyte. XPS scans of the **(c)** Si 2p and **(d)** Ti 2p regions before and after CA experiments using the high concentration MO_x|Ir electrodes.

SVII. Selectivity Calculations

The selectivity (taken at 1.65 V vs RHE) towards the OER over Fe(II) oxidation for each of the Ir-based electrodes in Fe-containing aqueous electrolyte was calculated using **Equation S1**,

$$S_D = \frac{r_D}{r_D + r_U} = \frac{i_D/n_D F}{\frac{i_D}{n_D F} + \frac{i_U}{n_U F}} = \frac{i_D}{i_D + (n_D/n_U * i_U)} = \frac{i_{tot} - i_U}{i_{tot} + (\frac{n_D}{n_U} - 1) i_U} \qquad \textbf{Equation S1}$$

Here, i_x is the partial current density of reaction x, n_x the electron transfer number of reaction x, F is the Faraday constant, and r_x represents the reaction rate of reaction x. Subscripts represents the total current density *tot*, the desired reaction *D* (OER), and the undesired reaction *U* (FeOR). Utilizing the fact that the only significant current density below 1.45 V vs. RHE is the Fe(II) reaction, the variable $i_{U,}$ was estimated by a linear extrapolation of the FeOR current taken over the region of 1.23 and 1.45 V vs RHE and extended to potentials >1.45V (**Figure S19**)

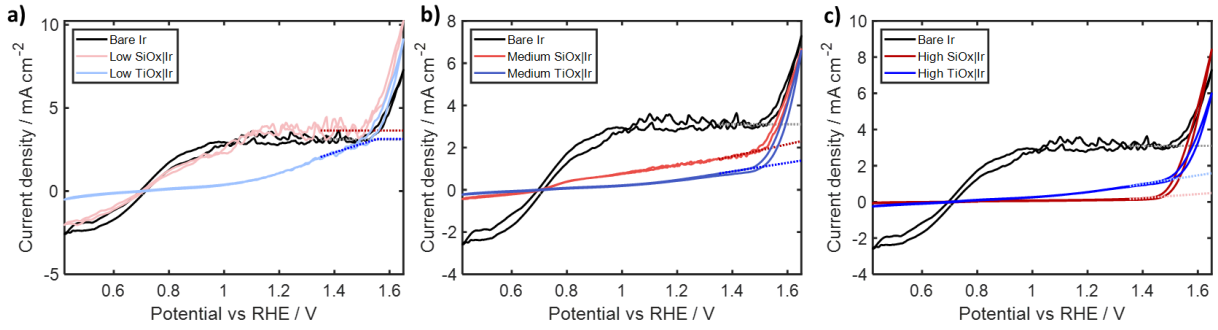

Figure S19: Cyclic voltammograms of **(a)** low, **(b)** medium and **(c)** high concentration SiO_x|Ir, TiO_x|Ir and bare Ir (black trace) electrodes. The dashed curves indicate an estimation of the FeOR partial current density based on the extrapolation of the measured FeOR current at potentials where the OER doesn't occur to potentials >1.45 V vs RHE.

SVIII. Electrical Conductivity Measurements

To assess the electrical conductivity of TiO_x and SiO_x overlayers in a wetted environment, a set of electrodes were constructed with a thin (≈ 1 nm) layer of Pt deposited on top of SiO_x|Pt|p+Si(100) and TiO_x|Pt|p+Si(100) electrodes to create a "sandwich structure" as illustrated in **Figure 5a** and described in the main article**.** Samples were mounted onto a rotator to better control the mass transport of reactant species, and experiments were completed at three different rotational rates in Fe-containing electrolyte composed of deaerated aqueous 0.1 M Na_2SO_4 + 50 mM H_2SO_4 + 25 mM $FeSO_4$ + 12.5 mM $Fe_2(SO_4)_3$ (pH adjusted to 1.5). Electrical resistance associated with the oxide interlayer in the sandwich structure electrodes was estimated by subtracting the CV curve for the bare Pt sample with the oxide encapsulated sample, as seen for a few examples in **Figure S20**. The linearity of the resulting curves is consistent with Ohm's law, which further confirms that the shifts in CV curves for the sandwich structure samples is associated with an ohmic drop associated with electron transport across the oxide interlayer to the outer Pt surface.

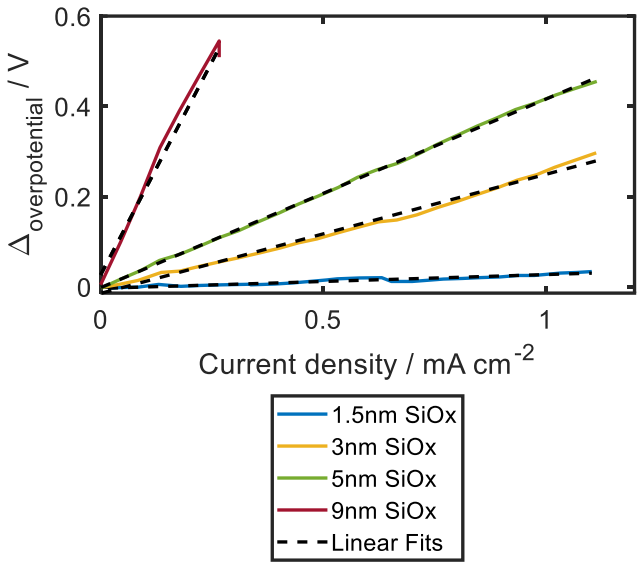

Figure S20. Calculated ohmic overpotentials (assumed to be ohmic drops across the oxide layer) of representative sandwich structure electrodes (Pt|MO_x|Pt) obtained by plotting the difference in potential of a bare platinum control electrode from the potential of Pt|SiO_x|Pt samples, plotted as a function of FeOR current density. Solid curves show the raw difference curves, while dashed curves represent linear fits to the difference curves, which were used to extract the ohmic resistance associated with the oxide interlayer as described in the text.

The total resistance for electron transport across an oxide layer (R) can be calculated from the slope of the overpotential vs. current density curves such as those shown in **Figure S21** based on Ohm's law. The calculated oxide layer resistances for each sample are plotted in **Figures S21a**. Finally, the oxide electronic resistivity can be calculated using **Equation S2**,

$$\rho = \frac{R \cdot A}{t_0} \qquad \textbf{Equation S2}$$

where ρ is the resistivity of the overlayer, t_0 is the thickness of the overlayer, and A is the cross-sectional area.

The resistivities of the overlayers were calculated at three rotational rates, as well as for the Fe(II) oxidation and the Fe(III) reduction reactions, with the results shown in **Figure S21b** and **Figure S22**, respectively.

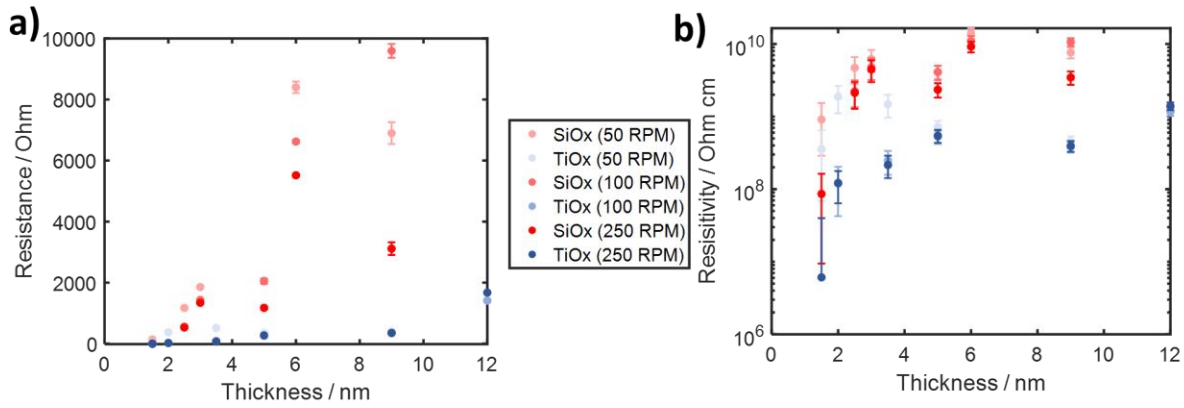

Figure S21. **(a)** Calculated electrical resistance (*R*) plotted as a function of overlayer thickness for Pt|MO_x|Pt samples mounted onto a rotator at three different rotation speeds (provided in revolutions per minute (RPM) for SiO_x (red) and TiO_x (blue) interlayers. **(b)** Resistivity values calculated using Equation S2 using the propagated error associated with the calculated slope and thickness measurements.

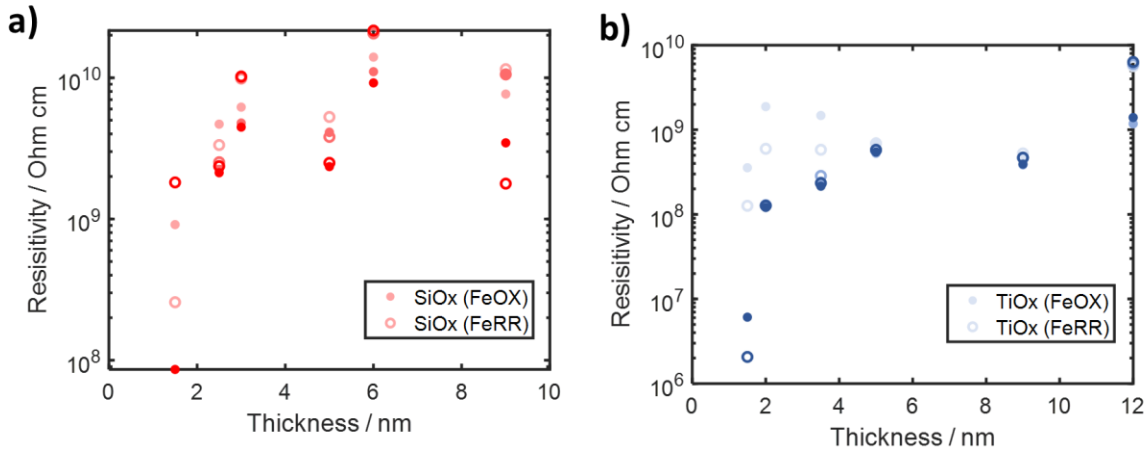

Figure S22. Calculated resistivity of oxide interlayers based on the Fe(II) oxidation reaction (FeOR) or Fe(III) reduction reaction (FeRR) for **(a)** Pt|SiO_x|Pt and **(b)** Pt|TiO_x|Pt at three different rotation speeds.

A Levich-style analysis was completed for all samples over the range of rotation speeds. For thin oxide interlayers, there was a linear relationship between current and the square root of rotation speed, suggesting that the recorded current is limited by diffusion of the Fe(II) or Fe(III) reactant across the diffusion boundary layer in the electrolyte. However, at larger oxide layer thicknesses, this trend deviated from linearity, suggesting that the current is no longer limited by mass-transport in the electrolyte (**Figure S23**).

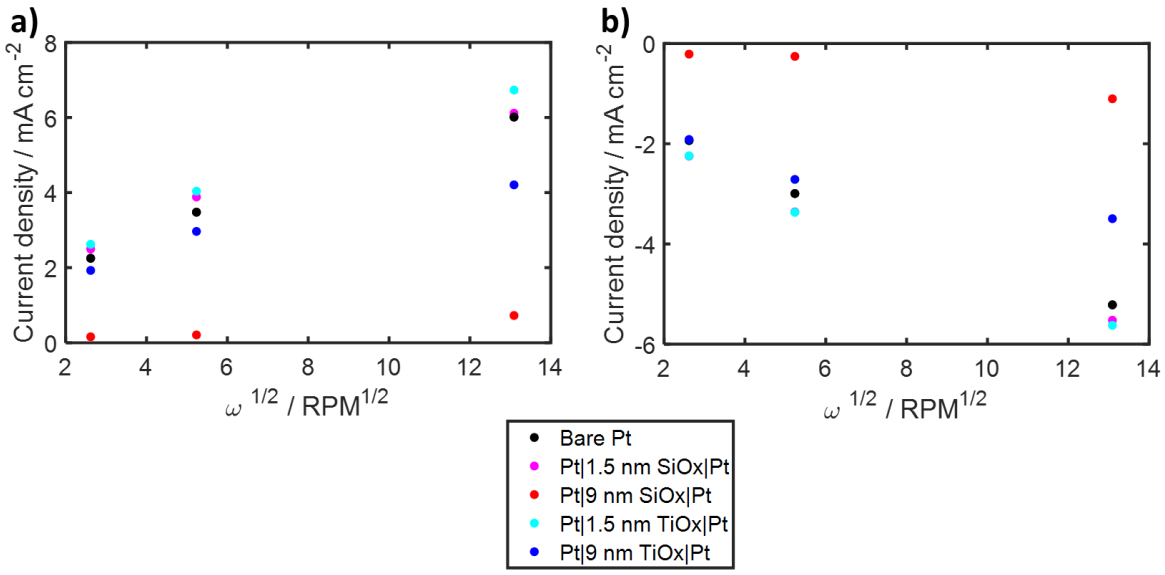

Figure S23: Levich plot, showing limiting current density vs square root of rotational rate, of Pt|MO_x|Pt electrodes of two different thicknesses for the **(a)** FeOR and the **(b)** FeRR.

This conclusion is corroborated by calculating the effective diffusion coefficient for Fe(II) and Fe(III) from the Levich equation seen in Equation S3[14]:

$$\frac{I_{l,A}}{A} = (0.620)nFD_A^{2/3}\nu^{-\frac{1}{6}}C_A\,\omega^{1/2} \qquad \textbf{Equation S3}$$

where $I_{l,A}$ is the mass-transport limiting current of species A, n is number of electrons, F is the Faraday constant, D_A is the diffusion coefficient of species A, v is the kinematic viscosity, C_A is the concentration of species A, and ω is the rotation rate. By plotting $I_{l,A}$ against $(\omega)^{1/2}$, a linear fit can be used to extract the diffusion coefficient of either Fe(II) or Fe(III). As seen in **Figure S24,** there is a large disagreement between the calculated diffusion coefficients and those from the literature[15] for the thicker oxide interlayers, suggesting that the measured current densities are limited by charge transport across the oxide layer, not diffusion of Fe(II) or Fe(III) across the diffusion boundary layer.

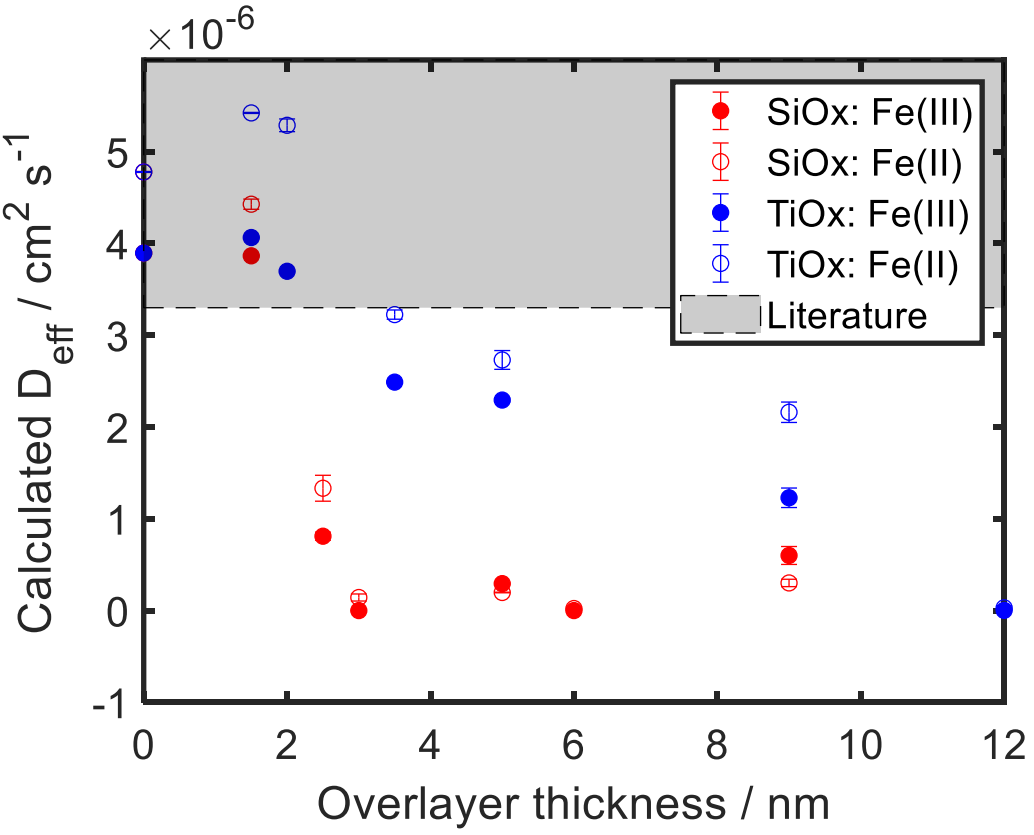

Figure S24. Calculated effective diffusion coefficient of Fe(III) and Fe(II) based on Equation S3 for overlayers with varying thickness. A range of literature values for the Fe(II)- and Fe(III)-sulfate complexes were considered from [15] and plotted as a grey region.

SIX. Cyclic Voltammograms of Bare Si Substrates

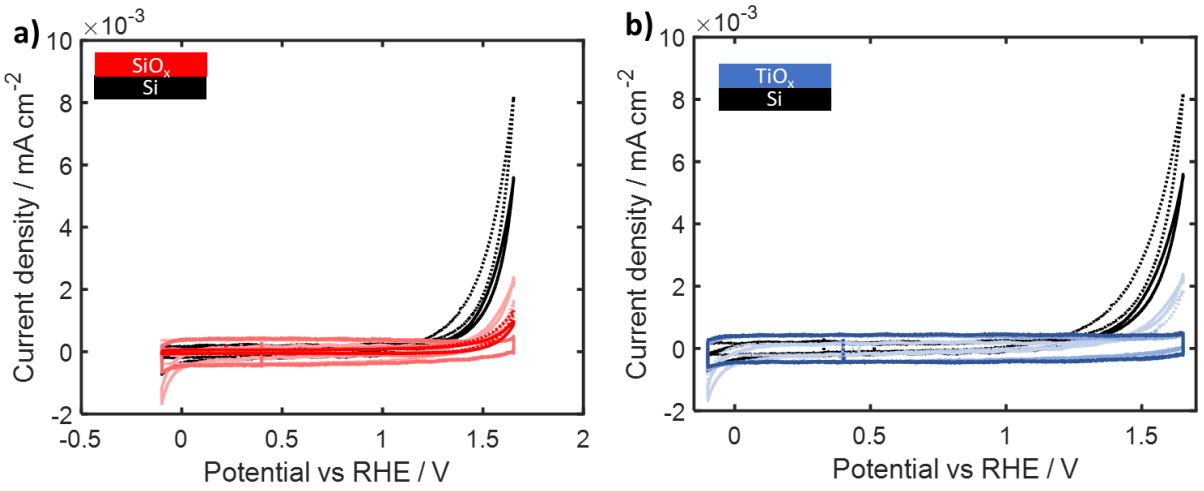

Figure S25. Representative CV cycles of **(a)** SiO_x|p+Si and **(b)** TiO_x|p+Si with a scan rate of 100 mV s^{-1} in deaerated aqueous supporting electrolyte (dotted line, 0.1 M Na_2SO_4 + 0.05 M H_2SO_4) and Fe-containing electrolyte (solid line, 25 mM $FeSO_4$ + 12.5 mM $Fe_2(SO_4)_3$). Black lines correspond to the bare p+Si substate, while colored lines with increasing darkness directly correlate to overlayer thickness (i.e., 2 nm, 5 nm, 10 nm).

SX. Comparison of FeRR limiting currents for ALD and UV-Ozone TiO_x coatings

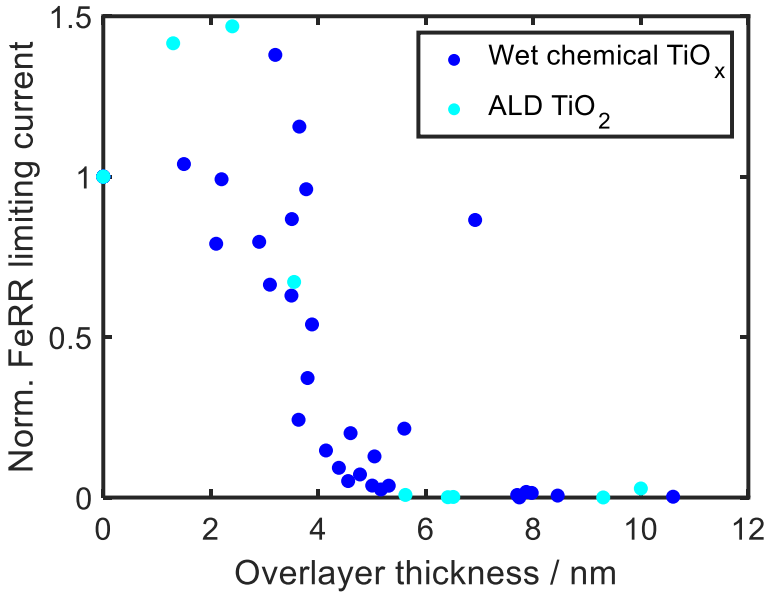

Figure S26. Limiting current for the Fe(III) reduction reaction (FeRR) plotted as a function of thickness (measured via ellipsometry) for both wet chemical TiO_2 (blue) and atomic layer deposited TiO_x (cyan), normalized against the limiting current for the bare control electrode. Limiting currents towards the FeRR were extracted from CV scans averaged over 0.45 – 0.5 V vs RHE in Fe-containing electrolyte composed of deaerated aqueous 0.1 M Na_2SO_4 + 50 mM H_2SO_4 + 25 mM $FeSO_4$ + 12.5 mM $Fe_2(SO_4)_3$ (pH adjusted to 1.5).

SXI. Cyclic voltammetry of MO_x|FTO

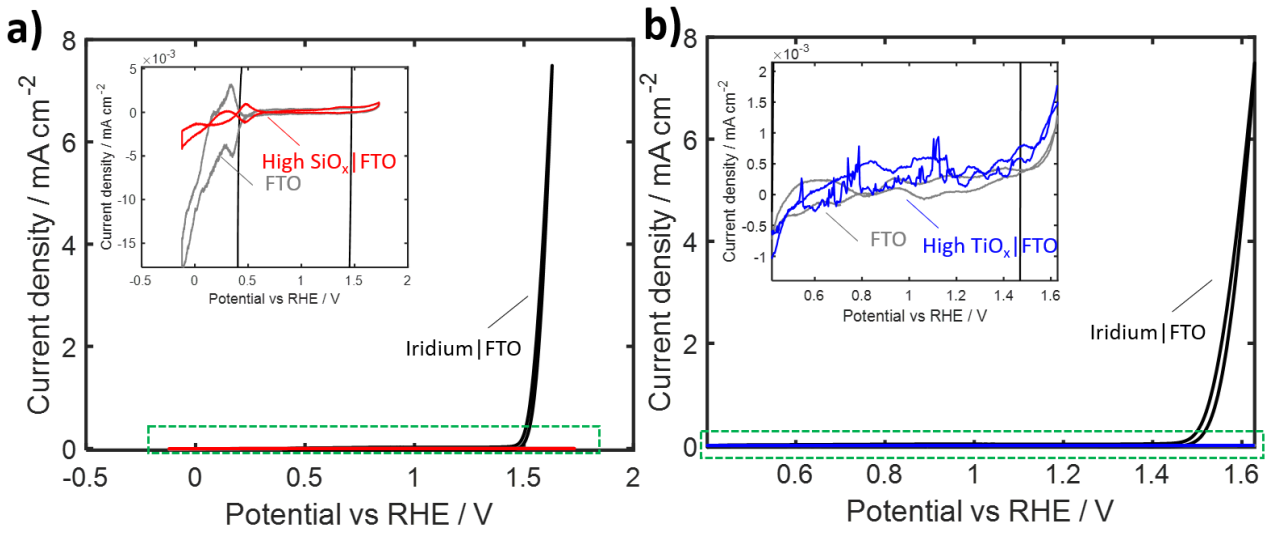

Figure S27. Representative CV cycles of high concentration **(a)** SiO_x|FTO and **(b)** TiO_x|FTO with a scan rate of 20 mV s^{-1} in deaerated aqueous supporting electrolyte (dotted line, 0.1 M Na_2SO_4 + 0.05 M H_2SO_4) Black and grey lines correspond to the bare Iridium|FTO and bare FTO substates respectively. Insets of lower y-axis scale (highlighted in green location) showcase minimal difference in OER activity as compared the bare FTO substrate.

SXII. References

1. S. Grazulis, D. Chateigner, R. T. Downs, A. F. T. Yokochi, M. Quiros, L. Lutterotti, E. Manakova, J. Butkus, P. Moeck and A. Le Bail, *Journal of Applied Crystallography*, 2009, **42**, 726-729.
2. T. M. Project, Materials Data on Ir by Materials Project, DOI: 10.17188/1186086.
3. L. Schick, R. Sanchis, V. González-Alfaro, S. Agouram, J. M. López, L. Torrente-Murciano, T. García and B. Solsona, *Chemical Engineering Journal*, 2019, **366**, 100-111.
4. J. J. Velasco-Vélez, T. E. Jones, V. Streibel, M. Hävecker, C. H. Chuang, L. Frevel, M. Plodinec, A. Centeno, A. Zurutuza, R. Wang, R. Arrigo, R. Mom, S. Hofmann, R. Schlögl and A. Knop-Gericke, *Surface Science*, 2019, **681**, 1-8.
5. S. J. Freakley, J. Ruiz-Esquius and D. J. Morgan, *Surface and Interface Analysis*, 2017, **49**, 794-799.
6. C. E. Finke, S. T. Omelchenko, J. T. Jasper, M. F. Lichterman, C. G. Read, S. Lewis and M. R. Hoffmann, *Energy & Environmental Science*, 2019, **12**, 358-365.
7. M. C. Biesinger, L. W. M. Lau, A. R. Gerson and R. S. C. Smart, *Applied Surface Science*, 2010, **257**, 887-898.
8. M. C. Biesinger, *Applied Surface Science*, 2022, **597**, 153681.
9. N. Y. Labrador, E. L. Songcuan, C. De Silva, H. Chen, S. J. Kurdziel, R. K. Ramachandran, C. Detavernier and D. V. Esposito, *ACS Catal.*, 2018, **8**, 1767-1778.
10. T. Reier, M. Oezaslan and P. Strasser, *ACS Catal.*, 2012, **2**, 1765-1772.
11. T. Shinagawa, A. T. Garcia-Esparza and K. Takanabe, *Scientific Reports*, 2015, **5**, 13801.
12. Y. Zhao, N. M. Vargas-Barbosa, E. A. Hernandez-Pagan and T. E. Mallouk, *Small*, 2011, **7**, 2087-2093.
13. M. Bernt, A. Siebel and H. A. Gasteiger, *Journal of The Electrochemical Society*, 2018, **165**, F305.
14. A. J. Bard, L. R. Faulkner and H. S. White, Wiley, 2022, vol. 3rd, ch. Microscopic Theories of Charge Transfer, pp. 142-168.
15. A. F. Gil, L. Galicia and I. González, *Journal of Electroanalytical Chemistry*, 1996, **417**, 129-134.